RESEARCH ARTICLE
SPACE PHYSICS: MAGNETOSPHERIC PHYSICS

Earth and Planetary Physics
8: 173–183, 2024
doi: 10.26464/epp2023069

Estimating the subsolar magnetopause position from soft X-ray images using a low-pass image filter

Hyangpyo Kim[1,2*], Hyunju K. Connor[3], Jaewoong Jung[3,4], Brian M. Walsh[5], David Sibeck[3], Kip D. Kuntz[6], Frederick S. Porter[3], Catriana K. Paw U[5], Rousseau A. Nutter[3,7], Ramiz Qudsi[5], Rumi Nakamura[1], and Michael Collier[3]

[1]Space Research Institute, Austrian Academy of Sciences, 8042 Graz, Austria;

[2]Geophysical Institute, University of Alaska Fairbanks, Fairbanks, Alaska 99775, USA;

[3]National Aeronautics and Space Administration (NASA) Goddard Space Flight Center, Greenbelt, Maryland 20771, USA;

[4]Astronomy Department, University of Maryland College Park, College Park, Maryland 20742, USA;

[5]Center for Space Physics, Boston University, Boston, Massachusetts 02215, USA;

[6]Department of Physics and Astronomy, Johns Hopkins University, Baltimore, Maryland 21218, USA;

[7]Howard University, Washington, DC 20059, USA

Key Points:

- We introduce a novel method in which we extract a subsolar magnetopause position from a LEXI (Lunar Environment heliospheric X-ray Imager) soft X-ray image by using a geometric equation and image filtering in the frequency domain.
- Our method estimates a subsolar magnetopause position with an accuracy of < 0.3 R_E when the solar wind density is overall >10 cm^{-3}, meeting the LEXI requirement.
- Our method captures the earthward magnetopause motion during the southward interplanetary magnetic field turning.

Citation: Kim, H., Connor, H. K., Jung, J., Walsh, B. M., Sibeck, D., Kuntz, K. D., Porter, F. S., Paw U, C. K., Nutter, R. A., Qudsi, R., Nakamura, R., and Collier, M. (2024). Estimating the subsolar magnetopause position from soft X-ray images using a low-pass image filter. *Earth Planet. Phys.*, *8*(1), 173–183. http://doi.org/10.26464/epp2023069

Abstract: The Lunar Environment heliospheric X-ray Imager (LEXI) and Solar wind Magnetosphere Ionosphere Link Explorer (SMILE) missions will image the Earth's dayside magnetopause and cusps in soft X-rays after their respective launches in the near future, to specify global magnetic reconnection modes for varying solar wind conditions. To support the success of these scientific missions, it is critical to develop techniques that extract the magnetopause locations from the observed soft X-ray images. In this research, we introduce a new geometric equation that calculates the subsolar magnetopause position (R_s) from a satellite position, the look direction of the instrument, and the angle at which the X-ray emission is maximized. Two assumptions are used in this method: (1) The look direction where soft X-ray emissions are maximized lies tangent to the magnetopause, and (2) the magnetopause surface near the subsolar point is almost spherical and thus R_s is nearly equal to the radius of the magnetopause curvature. We create synthetic soft X-ray images by using the Open Geospace General Circulation Model (OpenGGCM) global magnetohydrodynamic model, the galactic background, the instrument point spread function, and Poisson noise. We then apply the fast Fourier transform and Gaussian low-pass filters to the synthetic images to remove noise and obtain accurate look angles for the soft X-ray peaks. From the filtered images, we calculate R_s and its accuracy for different LEXI locations, look directions, and solar wind densities by using the OpenGGCM subsolar magnetopause location as ground truth. Our method estimates R_s with an accuracy of <0.3 R_E when the solar wind density exceeds >10 cm^{-3}. The accuracy improves for greater solar wind densities and during southward interplanetary magnetic fields. The method captures the magnetopause motion during southward interplanetary magnetic field turnings. Consequently, the technique will enable quantitative analysis of the magnetopause motion and help reveal the dayside reconnection modes for dynamic solar wind conditions. This technique will support the LEXI and SMILE missions in achieving their scientific objectives.

Keywords: soft X-ray; magnetopause; reconnection; low-pass filter; LEXI; SMILE

1. Introduction

The Earth's dayside magnetospheric system, namely the magnetosheath and cusps, emits soft X-rays as high-charge-state solar wind ions, such as O^{7+} exchange electrons, with the Earth's exospheric neutrals (e.g., Lisse et al., 1996; Cravens 1997; Walsh et al. 2016; Sibeck et al., 2018). The Roentgen SATellite mission (ROSAT; Trümper, 1982) discovered X-rays from the Earth's magnetosphere generated through this solar wind charge exchange process (Cravens et al. 2001). The X-ray Multi-Mirror

Correspondence to: H. Kim, Hyangpyo.kim@oeaw.ac.at
Received 10 MAY 2023; Accepted 15 NOV 2023.
First Published online 08 DEC 2023.

Mission (XMM-Newton; Jansen et al. 2001) observed strong emission of soft X-rays (0.05–2.0 keV) when it looked through the dayside magnetosphere (Carter et al., 2010, 2011), supporting the hypothesis that the magnetosheath is a strong soft X-ray emitter, as speculated by the modeling study of Robertson and Craven (2003). These observations provided substantial motivation to design future space missions that visualize the interaction between the solar wind and magnetosphere in soft X-rays. In this context, the Lunar Environment heliospheric X-ray Imager (LEXI; Walsh et al., 2020) and the Solar wind Magnetosphere Ionosphere Link Explorer (SMILE; Branduardi-Raymont et al., 2018) are scheduled to launch in 2024 and 2025, respectively.

The LEXI imager is one of 10 instruments to be deployed on the lunar surface by the Firefly Aerospace lunar lander under the National Aeronautics and Space Administration (NASA) Commercial Lunar Payload Services project. The LEXI imager will provide $9.1° \times 9.1°$ field-of-view (FOV) soft X-ray images of the dayside magnetosphere. The micropore optic telescope is sensitive to photons of 0.1–2.0 keV and has a focal length of 37.5 cm. Its operational period is less than 2 wk because of the harsh thermal environment during the lunar night. The SMILE is a joint European–Chinese mission that will be launched in 2025 into a highly ecliptic polar orbit with an apogee of ~19 R_E and an orbital period of ~50 h. The SMILE spacecraft will have four instruments on board: a Soft X-ray Imager (SXI), an aurora UV Imager (UVI), a Light Ion Analyzer (LIA), and a Magnetometer (MAG). The SMILE SXI will provide $15.5° \times 26.5°$ FOV images of the dayside magnetosphere for at least 40 continuous hours per orbit during its 3-year mission. The wide FOV soft X-ray images of LEXI and SMILE will observe how the Earth's magnetosheath and its boundaries move under dynamic solar wind conditions and will thus provide critical input into the nature of magnetopause reconnection.

Recently, various techniques have been developed to extract the magnetopause position from soft X-ray images (Collier and Connor 2018; Jorgensen et al., 2019a, b; Sun TR et al., 2020). Some of these utilize a limb-brightening effect, a phenomenon in which an object appears to become brighter toward its edges (e.g., Oiler and Rogers, 2020). A line-of-sight (LOS) tangent to the magnetopause has a longer path in the magnetosheath than do other LOSs. Because the Earth's magnetosheath emits soft X-rays, more soft X-rays are accumulated along this LOS. As a result, the magnetopause can be recognized as a curved line of peak emissions in the soft X-ray images. Collier and Connor (2018) and Sun TR et al. (2020) used these LOSs of peak emissions (i.e., tangent vectors to the magnetopause) to trace the magnetopause.

Collier and Connor (2018) introduced a technique that reconstructs the global three-dimensional (3D) magnetopause from two-dimensional (2D) soft X-ray images under steady solar wind conditions. First, they derived an equation to calculate the magnetopause position as a function of the spacecraft positions and the angles of soft X-ray emission peaks. They then simulated soft X-ray images expected from a virtual spacecraft by using a global magnetohydrodynamic (MHD) model. Finally, they extracted the magnetopause positions from the 2D images by using their analytical magnetopause equation. The results showed good agreement with the magnetopause positions obtained from the MHD model.

Sun TR et al. (2020) introduced another magnetopause tracing technique that uses the limb-brightening effect. First, they defined a function for the magnetopause shape similar to the one by Shue et al. (1997) and created a chart of various magnetopause positions. Second, they simulated the soft X-ray image expected from a virtual satellite by using a global MHD model and obtained the magnetopause curve by connecting the peak emission pixels in the image. Third, they investigated which magnetopause in their chart created a similar magnetopause curve in the soft X-ray image. Finally, they concluded that the real magnetopause position was the same as the magnetopause shape on their chart that gave the best-match curve to the curve in the satellite image. Their tracing results showed good agreement with the MHD magnetopause locations.

Collier and Connor (2018) and Sun TR et al. (2020) used ideal soft X-ray images so that the peak emission angles could be easily identified. However, a real soft X-ray image is not smooth because of various X-ray sources in the sky, the instrumental background, and Poisson noise (Sibeck et al. 2018; Jung et al. 2022). It is not always easy to obtain accurate peak emission angles from real soft X-ray images with moderate signal-to-noise ratios, which creates an additional challenge for magnetopause tracing. In this work, we introduce a novel method that estimates subsolar magnetopause positions from synthetic soft X-ray images by using a new geometric equation and image filtering. We apply this technique to synthetic soft X-ray images from LEXI, but our technique is equally applicable to images from SMILE or other future soft X-ray imaging missions positioned outside the magnetosphere.

Section 2 describes how we simulate synthetic soft X-ray images from a global MHD model and trace the subsolar magnetopause locations from the images. Section 3 validates our tracing method for various LEXI locations, look directions, and solar wind conditions by using the magnetopause positions obtained from the MHD model as ground truth. Finally, Section 4 summarizes our results and presents concluding remarks.

2. Methodology

2.1 Simulation of Near-Earth Soft X-ray Emissions

To simulate near-Earth soft X-rays, we use the Open Geospace Global Circulation Model (OpenGGCM), a global magnetosphere–ionosphere model that solves resistive MHD equations with current-driven resistivities in nonuniform Cartesian grids. Its simulation box covers from ~−20 to 500 to ~1000 R_E along the X-axis and from −45 to 45 R_E along the Y- and Z-axes in Geocentric Solar Ecliptic (GSE) coordinates. The OpenGGCM uses solar wind plasma moments and interplanetary magnetic fields (IMF) as input and provides the plasma density, velocity, temperature, and electromagnetic fields as output. Details of the OpenGGCM and its applications to the geospace research can be found in Raeder et al. (2001, 2008), Connor et al. (2012, 2014, 2015, 2016, 2021), Oliveira and Raeder (2015), Ferdousi and Raeder (2016), Cramer et al. (2017), Jensen et al. (2017), Shi Y et al. (2017), Kavosi et al. (2018), Ferdousi et al. (2021), and (Jung et al. 2022).

We also use the simple exospheric neutral density model from Cravens et al. (2001) to obtain the neutral hydrogen density (n_n):

$$n_n = 25\left(\frac{10R_E}{R}\right)^3, \quad (1)$$

where n_n is in cm^{-3}, R is the radial distance from the Earth's center in units of Earth radius (R_E).

The soft X-ray emissivity along the LOS (R_x) is expressed as the line integral of the product of the plasma density (n_p), exospheric neutral density (n_n), relative velocity of the neutrals and ions (v_{rel}), and an effective scale factor (ς):

$$R_x = \frac{\varsigma}{4\pi}\int n_p n_n v_{rel}\mathrm{d}l, \quad (2)$$

$$v_{rel} = \sqrt{v_p^2 + v_{th}^2} = \sqrt{v_p^2 + \frac{3k_BT}{m}}, \quad (3)$$

where R_x is in $\left[\mathrm{eV\ cm^{-2}s^{-1}sr^{-1}}\right]$; v_p and v_{th} are the plasma bulk and thermal speeds, T is the plasma temperature, k_B is the Boltzmann constant, m is the proton mass, and dl is an infinitesimal length along the line of sight (LOS) of a soft X-ray detector (Cravens et al., 2001; Kuntz et al., 2015; Sibeck et al., 2018; Sun TR et al., 2020; Connor et al., 2021). Exospheric neutrals originate from the Earth's upper atmosphere, with typical energies of ~0.1 eV or 1000 K (Qin JQ and Waldrop 2016). The velocities of neutrals are expected to be much smaller than those of the magnetosheath plasma, whose typical energy ranges from hundreds of electron volts to several kiloelectron volts. Thus, the relative velocities (v_{rel}) are set with only plasma parameters. The OpenGGCM MHD model provides the plasma parameters (n_p and v_{rel}), and the exospheric density model provides the exospheric neutral density (n_n). The effective scale factor (ς) is determined by the charge-exchange cross sections, the energies of the soft X-ray emission lines, and the abundance of soft X-ray source plasmas in the solar wind (Whittaker and Sembay, 2016). The exact value of ς remains an active field of research because of the lack of observations and theoretical understanding of the dependent parameters.

Equation (2) simplifies to

$$R_x = \frac{\varsigma}{4\pi}Q, \quad (4)$$

where

$$Q = \int n_p n_n v_{rel}\mathrm{d}l, \quad (5)$$

where Q is in $\left[\mathrm{cm^{-4}\ s^{-1}}\right]$. Kuntz et al. (2015) calculated a conversion factor from Q to instrument count rates by comparing the ROSAT soft X-ray observations with the Q_s calculated along the ROSAT LOS from a global MHD model. With their conversion factor, Q directly transforms to count rates in the ROSAT ¼ keV band without using ς:

$$\text{ROSAT counts}\left[\mathrm{deg^{-2}\ s^{-1}}\right] = Q\times 3.86\times 10^{-20}\ \text{counts}\left[\mathrm{cm^4\ deg^{-2}}\right]. \quad (6)$$

The conversion ratio from the ROSAT to the LEXI count rate is estimated to be 0.03149. By multiplying this ratio to Equation (6), the LEXI count rate is expressed as a function of Q:

$$\text{LEXI counts}\left[\mathrm{deg^{-2}\ s^{-1}}\right] = Q\times 1.22\times 10^{-21}\text{counts}\left[\mathrm{cm^4\ deg^{-2}}\right]. \quad (7)$$

2.2 Derivation of the R_s Equation

We derive an equation that estimates the geocentric distance to the subsolar magnetopause (R_s) from soft X-ray images and the position of the spacecraft that takes the image. First, we assume that (1) the look direction of the maximum soft X-ray emission is tangent to the magnetopause (Collier and Connor 2018) and (2) the magnetopause near the subsolar point is nearly spherical and thus R_s is almost the same as the radius of the magnetopause curvature (D) (Sibeck et al. 1991). Under those assumptions, we can estimate R_s with a satellite location ($\boldsymbol{S}$), a look direction for the center of the soft X-ray image ($\boldsymbol{L}$), and an angle for the soft X-ray peak emission away from $\boldsymbol{L}$ (α):

$$R_s \approx D = \boldsymbol{S}\sin\lambda, \quad (8)$$

$$\lambda = \cos^{-1}\left[\frac{\left(|\boldsymbol{S}|^2 + |\boldsymbol{S}-\boldsymbol{L}|^2 - |\boldsymbol{L}|^2\right)}{2\,|\boldsymbol{S}|\,|\boldsymbol{S}-\boldsymbol{L}|}\right] \pm \alpha. \quad (9)$$

The law of cosines is used for Equation (9). Figure 1 illustrates the R_s derivation geometry on a GSE XY plane. If LEXI location ($\boldsymbol{S}$) and pointing ($\boldsymbol{L}$) are known and our two assumptions are satisfied, the accuracy of R_s is determined by the soft X-ray peak emission angle (α).

We validate Equation (8) by tracing R_s from ideal soft X-ray images from LEXI and comparing the R_s estimates with the OpenGGCM subsolar magnetopause positions. First, we conduct the OpenGGCM simulation for a southward IMF of −4 nT, a flow speed of 400 km/s along the GSE X-axis, and a solar wind density of 10 cm^{-3} and calculate the soft X-ray images expected from LEXI. Figure 2a shows a global image of the dayside magnetosphere in soft X-rays for an observer looking at $\boldsymbol{L} = (11.65,\ 0,\ 0)\,R_E$ from

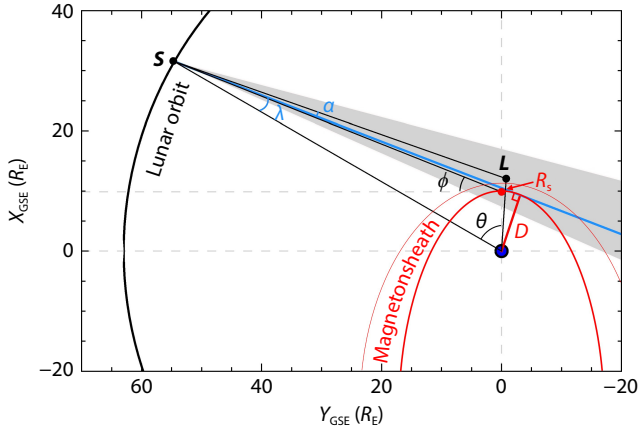

Figure 1. Derivation of R_s on a GSE XY plane by using the LEXI location ($\boldsymbol{S}$), look direction ($\boldsymbol{L}$), and soft X-ray peak emission angle (α). The LEXI spacecraft is located at $\boldsymbol{S} = (31.6, 54.73, 2.03)\ R_E$ and $\theta = 60°$, where θ is an angle from the Sun–Earth line to the satellite location. The LEXI imager has a 9.1° × 9.1° FOV (gray shading) with its center looking at $\boldsymbol{L} = (12.06, -0.77, 0.17)\,R_E$. The red curves indicate the bow shock and the magnetopause, and D is the radius of the magnetopause curvature under the second assumption, nearly the same as R_s. The blue line indicates the line tangent to the magnetopause, which is the look direction for the maximum soft X-ray count rate in the soft X-ray image.

$\boldsymbol{S}$ = (11, 62.34, −0.05) R_E and θ = 80°. Each 0.25° × 0.25° pixel of the image provides an LOS-integrated soft X-ray count for a 5-min exposure. No noise or other X-ray sources are included in this ideal image. Figure 2b shows soft X-ray images within the LEXI FOV for three different LEXI locations. Note that all the θ (or $\boldsymbol{S}$) and $\boldsymbol{L}$ change as LEXI moves. The white dashed lines are cuts at Z = 0°, and the soft X-ray count rates along these cuts are shown in the bottom panel. The colored dots indicate the angle of the soft X-ray peak emission (α) along Z = 0°. We calculate R_s from each image by using Equation (8) and estimate the R_s accuracy (σ) by using the OpenGGCM subsolar magnetopause position as ground truth (R_g). We define R_g as the location of the maximum plasma density gradient along the Sun–Earth line and σ as $|R_s - R_g|$. For the given solar wind conditions, R_g is located at 8.85 R_E, and our method can locate R_s with σ of < 0.33 R_E. The σ improves as the look direction of the maximum soft X-ray emission becomes parallel to a line perpendicular to the Sun–Earth line. We define ϕ as the angle of the LEXI–R_s line estimated from the perpendicular line (see Figure 1). Here, ϕ = 0° means that the peak emission angle is nearly tangent to a subsolar magnetopause point (R_s), not some other magnetopause region; thus, the radius of the magnetopause curvature (D) is almost the same as R_s. The LEXI imager aims to extract the magnetopause location within a 0.3 R_E resolution from a soft X-ray image with a 5-min exposure time. Our method can trace the subsolar magnetopause position with an accuracy comparable to or less than the LEXI requirement.

2.3 Calculation of a Realistic Soft X-ray Image

Although Equation (8) provides accurate R_s estimates, it needs to be further validated because real X-ray images are not smooth, as shown in Figure 2b, owing to other X-ray sources in the sky, the telescope response to photons, and noise (Sibeck et al., 2018). Hence, we need to test the performance of our technique to take into account noisy soft X-ray images.

We create synthetic soft X-ray images by considering a constant galactic background, the LEXI instrument response, and Poisson noise. Figure 3 schematically shows the imaging process, going from an ideal soft X-ray image to a synthetic soft X-ray image. Figure 3a shows an ideal image for the near-Earth solar wind charge exchange emission, the same as in Figure 2b. We add a uniform galactic background of 0.27 counts/pix/s to all the pixels in Figure 3a and then divide the total counts (i.e., near-Earth X-ray + galactic background) by 1.6 to take into account the LEXI optics and filter performance. By including this uniform background, we can obtain total X-ray count rates closer to reality and thus create Poisson noise at a reasonable level. Figure 3b shows the total soft X-ray count rates that arrive at the LEXI detector after passing its optics. Focused optical imaging systems, such as telescopes and microscopes, always blur images of actual objects, and a point spread function (PSF) describes this blurred pattern. We convolve the total soft X-ray counts in Figure 3b with the LEXI PSF. This convolution slightly reduces the number of counts, as shown in Figure 3c. Assuming that the uncertainty in the number of counts is given by the Poisson distribution (Sibeck et al., 2018), we add random Poisson noise to Figure 3c and obtain the realistic LEXI soft X-ray image in Figure 3d. As described in the following section, we conduct the R_s accuracy test by using realistic soft X-ray images like the one in Figure 3d.

Note that we simplify the calculation of synthetic images. The actual sky background is not uniform, and the instrument background is not considered. However, the sky background is relatively well known from the ROSAT all-sky survey (Snowden et al., 1997), and the instrument background will be obtained through the upcoming LEXI calibration. We can subtract these backgrounds from the actual X-ray images. The processed LEXI images after

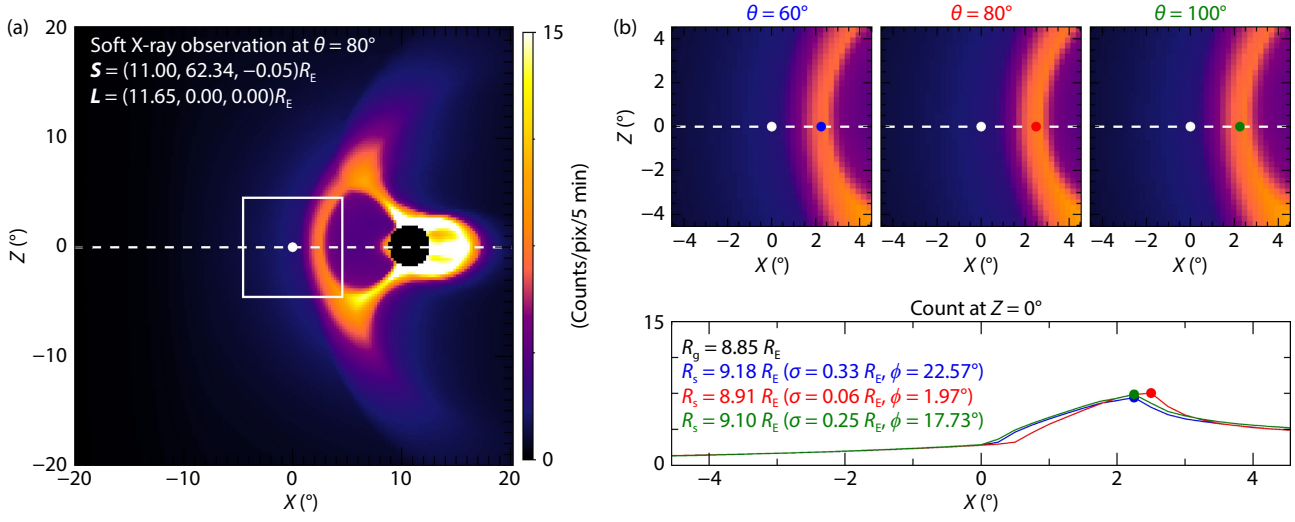

Figure 2. Ideal soft X-ray images from LEXI created with the OpenGGCM MHD model. Images are made with a pixel size of 0.25° × 0.25° and a exposure time of 5 min. (a) Global image in a large FOV. The white dot and square indicate the LEXI look direction $\boldsymbol{L}$ and FOV, repectively. (b) Top: Soft X-ray images in the LEXI FOV (9.1° × 9.1°) at different locations (θ and $\boldsymbol{S}$). The white dashed line is the Sun–Earth line, where Z = 0°, and the colored dots indicate the angle of the soft X-ray peak emission (α). Bottom: Soft X-ray count rate along the white dashed Sun–Earth lines labeled with the subsolar magnetopause position (R_s), the accuracy (σ), and the angle of the LEXI–R_s line estimated from a line perpendicular to the Sun–Earth line (ϕ).

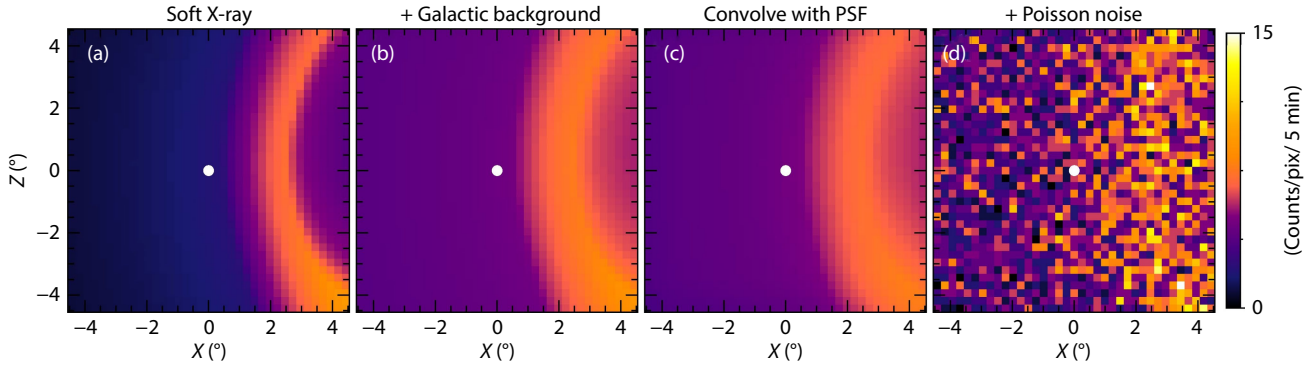

Figure 3. Imaging process used to construct a synthetic LEXI soft X-ray image.

removal of this background are expected to be similar to our synthetic images, like the one in Figure 3d. Our technique can be applied to these processed images. Details for realistic image calculation can be found in Sibeck et al. (2018) and the references therein.

2.4 Image Filtering in the Frequency Domain

It is challenging to determine an accurate soft X-ray peak angle (α) from noisy soft X-ray images. For example, Figure 4 shows an accuracy test for synthetic soft X-ray images in the same format as Figure 2b. We create the synthetic images by using the ideal images in Figure 2b. The X-ray count rates do not vary monotonically along the Sun–Earth line because of noise. The peak X-ray angles α (colored dots) lie far from those in Figure 2b, leading to significant error in $R_s(\sigma)$, larger than 0.88 R_E.

To obtain an accurate α, we remove background noise in the LEXI soft X-ray image by filtering in the frequency domain. The Fourier transform converts an original image in the spatial domain to an image in the frequency domain. An image in the low-frequency region typically corresponds to an overall outline of the original image, whereas an image in the high-frequency region corresponds to fine details of the original image. The low-pass Gaussian filter is widely used to eliminate high-frequency features, remove noise, and detect edges (e.g., Fabian et al., 2003; Sanders et al., 2016; Misra et al., 2018).

Figure 5 shows the filtering process used on a LEXI soft X-ray image. Figure 5a is the synthetic soft X-ray image, and Figure 5b is that image in the frequency domain after the 2-D fast Fourier transform. The main information in the image is distributed in the center, where low-frequency features reside. Next, we create a Gaussian low-pass filter $G(x, y)$ with the same size as our soft X-ray image (Figure 5c):

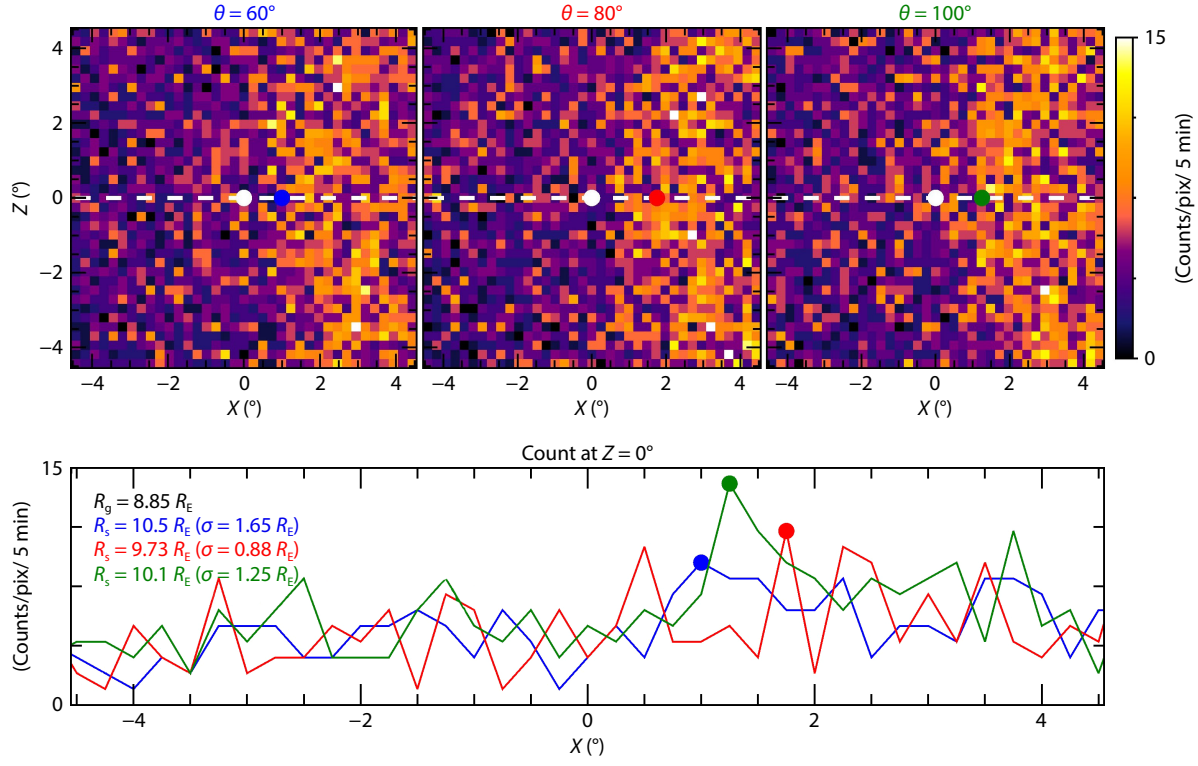

Figure 4. Accuracy test for synthetic soft X-ray images in the same format as Figure 2b.

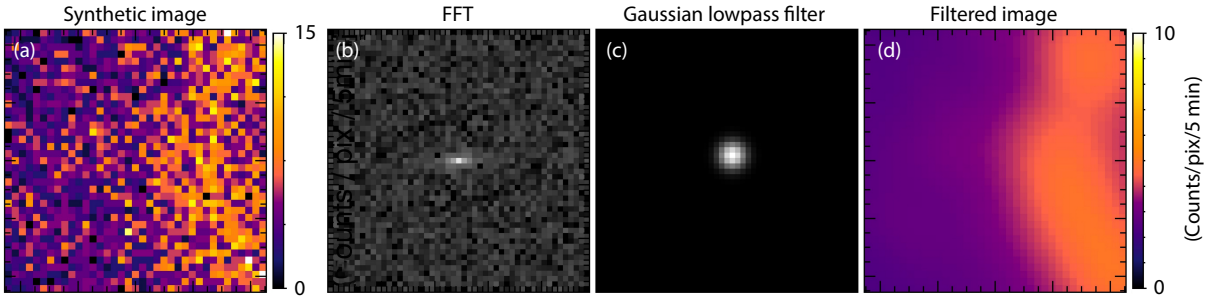

Figure 5. Process of filtering a synthetic soft X-ray image by using the fast Fourier transform (FFT) and a Gaussian low-pass filter. (a) Simulated synthetic image, (b) fast Fourier-transformed synthetic image (a), (c) image of the Gaussian low-pass filter, and (d) Gaussian filtered image.

$$G(x,y) = \exp\left(-\frac{d(x,y)^2}{2f_c^2}\right), \tag{10}$$

where $d(x, y)$ are the Euclidean distances from the image center and f_c is the cutoff spatial frequency corresponding to the standard deviation of $G(x, y)$. In the present study, we normalized d to have a value between 0 and 1, and we set f_c = 0.05 because the image features below f_c mostly correspond to the magnetosheath in the ideal image. We multiply this Gaussian low-pass filter in Figure 5c to the Fourier transformed image in Figure 5b, and then transform the filtered images in the frequency domain back to the spatial domain (i.e., inverse Fourier transform). Figure 5d shows the final filtered image in the spatial domain. This image is consequently blurred, but the magnetosheath boundaries are distinguished more clearly than in the original image in Figure 5a, which allows us to readily determine α.

3. R_s Accuracy Test

We now estimate how well our magnetopause tracing technique performs with the filtered LEXI images. Figure 6 shows an example of R_s estimation. The top and middle panels show synthetic soft X-ray images and those after Gaussian low-pass filtering, respectively. The bottom panel indicates the soft X-ray count rates along the Sun–Earth line in the filtered images. After this process, the count rates in the images vary smoothly and the soft X-ray peak angle (α) is readily obtained. The resultant R_s accuracy or error (σ) is significantly improved (<0.22) compared with the previous analysis in Figure 4, which utilizes only synthetic soft X-ray images.

We now estimate σ for various solar wind densities with a flow velocity of 400 km/s and different LEXI locations (θ = 60°–120°). Figure 7a shows the NASA OMNI solar wind proton density (n_{sw}) from 2011 to 2022. Because n_{sw} is typically observed between 1 and 20 cm^{-3}, we estimate σ for n_{sw} of 1, 5, 10, 15, and 20 cm^{-3}. The accuracy obtained in Figure 6 may not represent the typical performance of our technique because Poisson noise occurs randomly. To understand the average performance of our techniques, we produce 1000 synthetic images from a single ideal X-ray image by using 1000 trials of random Poisson noise distribution and calculating the average accuracy and its standard deviation. Figure 7b shows σ as a function of n_{sw} and θ (colors) for both the southward and northward IMF. The error bars indicate the standard deviation of σ for each n_{sw}. The black horizontal lines indicate the LEXI requirement to detect the magnetopause with $\sigma < 0.3\ R_E$ from a 5-min-exposed soft X-ray image.

Overall, σ improves with increasing n_{sw} and is better for the southward IMF than for the northward IMF. This is because the high signal-to-noise ratio of soft X-ray images is expected for strong n_{sw} and the southward IMF. A stronger n_{sw} indicates more X-ray source ions in the solar wind because the density of emitting ions is proportional to that of protons. For the southward IMF, the magnetopause erodes and the magnetosheath moves earthward, where the neutral density (n_n) is higher. Consequently, the charge exchange between solar wind ions and exospheric neutrals increases for a strong n_{sw} and the southward IMF. This exchange produces more soft X-ray photons, increases the signal-to-noise ratio of the soft X-ray images, and eventually improves σ. Our technique meets the LEXI required accuracy of $\sigma < 0.3\ R_E$ for $n_{sw} > 10$ cm^{-3} when LEXI is located at θ = 60°–100° (70°–90°) for the southward (northward) IMF orientation. The σ gets worse as LEXI moves deeply into the nightside region (larger θ). At these LEXI locations, the soft X-ray peak angle lies tangent to the flank magnetopause. Our assumption of a spherical magnetopause shape becomes less valid in this region, decreasing the accuracy of R_s.

The magnetopause motion provides important information on the mode of the dayside reconnection. The LEXI imager can reveal whether the reconnection happens globally or locally, fast or slow, and steadily or intermittently by observing the magnetopause motion from soft X-ray images. We test whether our tracing method can trace the magnetopause motion when the IMF rotates from northward to southward. To consider time-varying X-ray emission patterns, we calculate near-Earth X-ray counts every minute with 1-min exposure, accumulate the X-ray counts for the past 5 min, and finally obtain an ideal near-Earth soft X-ray image every 5 min with 5-min exposure. We then create 1000 synthetic images from the ideal soft X-ray image by introducing 1000 random trials with Poisson noise distributions, smooth the 1000 synthetic images by applying the image filtering as described in Figure 5, and obtain R_s estimates from the 1000 filtered images. Finally, we calculate the average and standard deviation of the R_s estimates by considering the OpenGGCM subsolar magnetopause position (R_g) as ground truth.

Figure 8 shows the test results. The top panel shows the IMF B_z at a 5-min resolution under a constant solar wind density of 10 cm^{-3} and a flow speed of 400 km/s. The IMF B_z is initially set at 5 nT and then turns to −5 nT after 03:40 universal time (UT). The bottom panels show R_g (gray lines) and R_s averaged from the 1000 R_s esti-

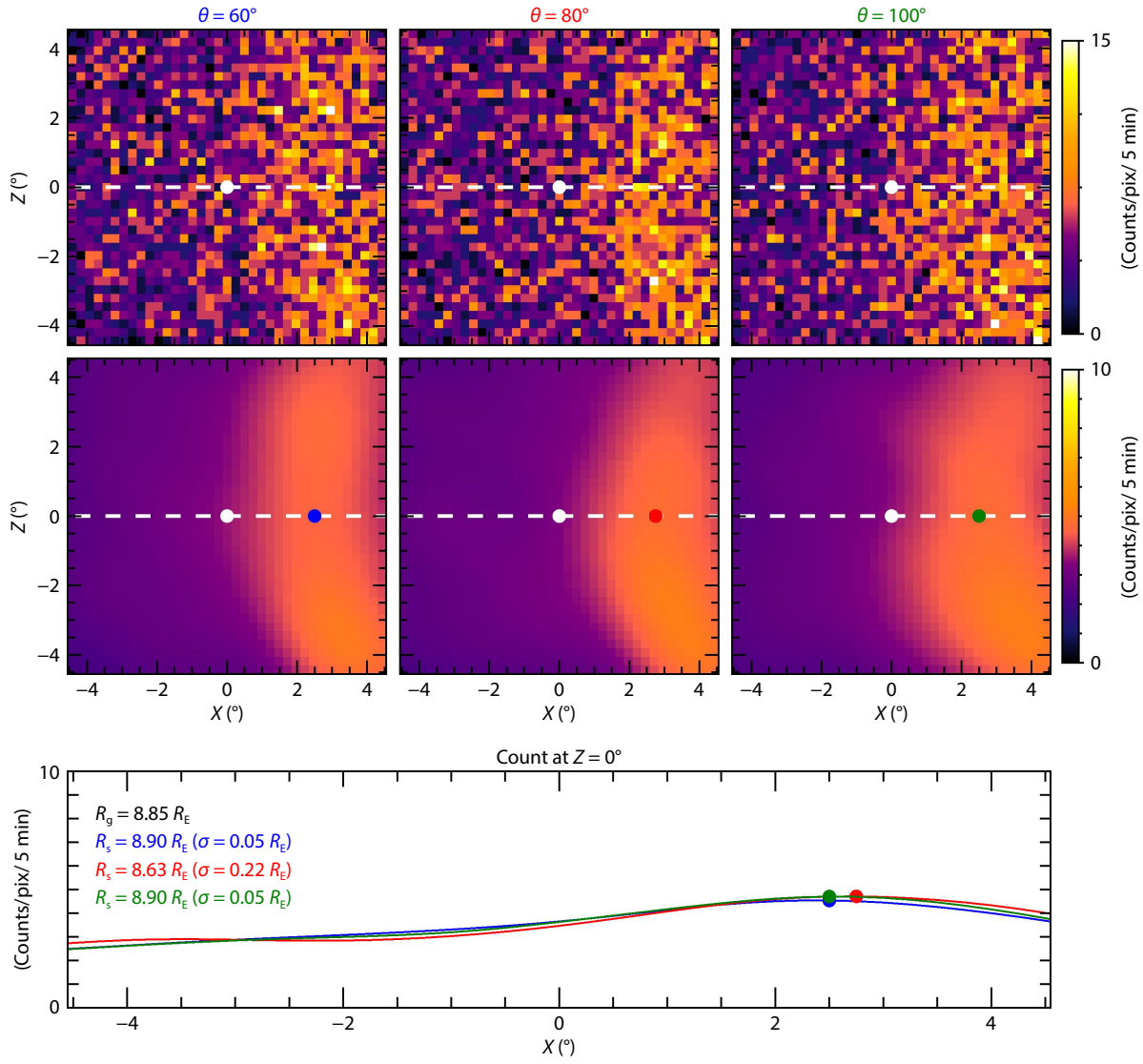

Figure 6. Accuracy test for the filtered soft X-ray images. The top and middle panels present the synthetic and filtered LEXI images, and the bottom panel shows count rates along the white dashed line in the filtered images.

mates (colored lines) for various LEXI locations. We also calculate the average σ for the entire period ($\bar{\sigma}$). The R_g stays at 9.7 R_E during the northward IMF and then begins to decrease after southward turning of the IMF as the dayside reconnection erodes the magnetopause. The R_g finally reaches 8.7 R_E. The magnetopause moves earthward by 1 R_E during this period. The R_s also decreases after the IMF turning, similar to R_g, even when LEXI lies in a nightside region (θ = 100°–120°) and provides a less optimal viewing point. The standard deviations (the error bars) are smaller than 1 R_E for all LEXI locations. The discrepancies between R_g and R_s are partly because the radius of the magnetopause curvature does not precisely match the actual subsolar magnetopause position and partly because LEXI is not at an optical location to observe the subsolar magnetopause, especially when it stays in the nightside region. Additionally, the use of a low-pass filter introduces a phase-shifting effect that can further lead to discrepancies. Despite these limitations, our tracing method reasonably captures the magnetopause motion and the trend in its variation during the continuous magnetic reconnection for a given solar wind condition.

4. Summary and Conclusions

In this article, we introduced and validated a new technique that traces a subsolar magnetopause position from a synthetic LEXI soft X-ray image. We derived an equation for the subsolar magnetopause position as a function of the satellite location, the look direction, and the angle of maximum soft X-ray emission under two assumptions: (1) that the look direction of the maximum soft X-ray emission lies tangent to the magnetopause, and (2) that the magnetopause near a subsolar point is nearly spherical. We created synthetic soft X-ray images with a uniform galactic background, a PSF, and random Poisson noise. To overcome the background noise in the synthetic soft X-ray image, we filtered the image in the frequency domain by using a Gaussian low-pass filter with a cutoff frequency of 0.05. We then estimated the subsolar magnetopause position and its accuracy for various solar wind densities and different LEXI locations. Our tracing method estimated the subsolar magnetopause position with an accuracy of $< 0.3\ R_E$ when the solar wind density exceeded >10 cm^{-3}, meeting

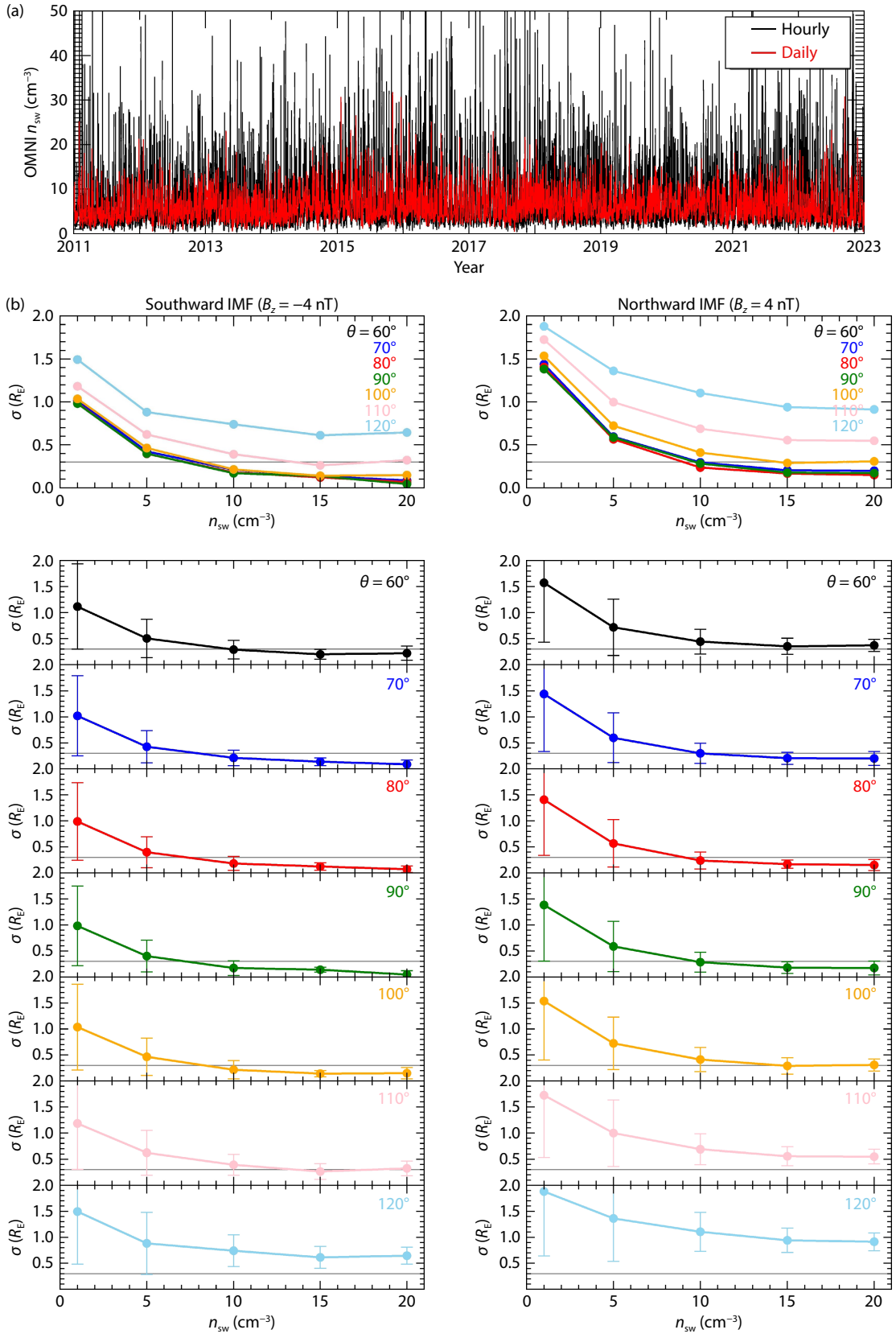

Figure 7. (a) OMNI solar wind proton density from 2011 to 2022. (b) Accuracy test for various solar wind densities (n_{sw}) and LEXI locations (θ) during the southward (left) and northward (right) IMF. The total effective area or signal-to-noise ratio is based on a LEXI-sized telescope. The gray horizontal lines indicate the required LEXI accuracy of 0.3 R_E.

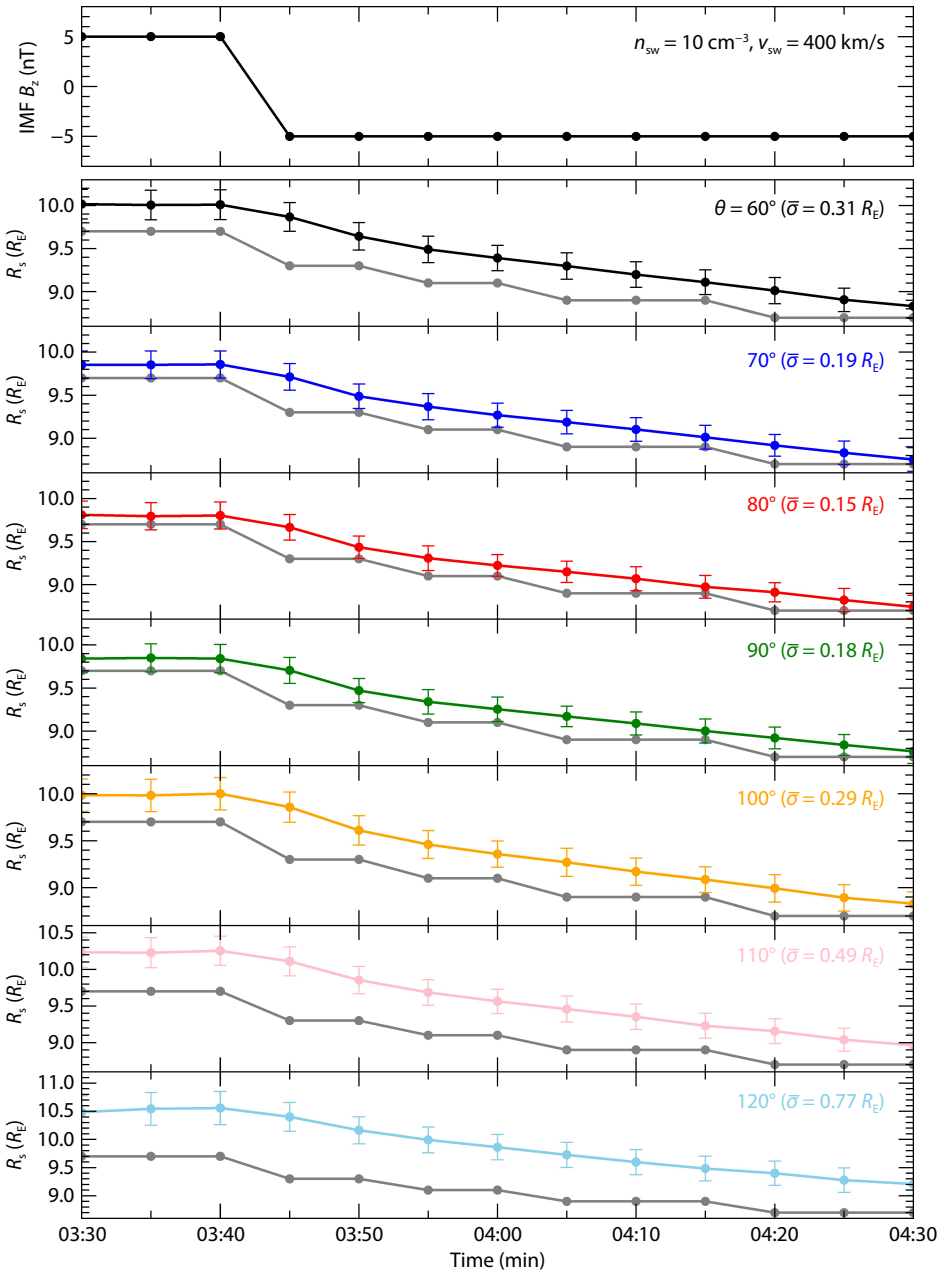

Figure 8. Magnetopause motion captured during the northward-to-southward IMF turning for different LEXI locations. The top panel shows the solar wind–IMF conditions, and the bottom panels compare our R_s estimates (colored lines with error bars) with the ground truth (gray lines).

the LEXI requirement. The accuracy improved as the solar wind density increased and during the southward IMF. Although the accuracy diminished when LEXI moved to the nightside region, we confirmed that our method was able to capture the motion of the magnetopause during continuous magnetic reconnection after the southward turning of the IMF. This performance is based on that of LEXI images and could improve for a larger image. Our tracing method is equally applicable to the SMILE soft X-ray images taken from a highly ecliptic polar orbit. Our technique enables us to analyze the magnetopause motion quantitatively and reveal the dayside reconnection modes for dynamic solar wind and IMF conditions, thus supporting successful scientific closure for upcoming LOS X-ray imaging missions, such as LEXI and SMILE.

Acknowledgments

This work was supported by NASA (Grant Nos. 80NSSC19K0844, 80NSSC20K1670, 80MSFC20C0019, and 80GSFC21M0002). HC gratefully acknowledges support from NASA Goddard Space Flight Center internal funding programs (HIF, Internal Scientist Funding Model, and Internal Research and Development).

References

Branduardi-Raymont, G., Wang, C., Escoubet, C. P., Adamovic, M., Agnolon, D., Berthomier, M., Carter, J. A., Chen, W., Colangeli, L., … Zhu, Z. (2018). SMILE definition study report (red book). ESA/SCI. https://sci.esa.int/web/smile/-/61194-smile-definition-study-report-red-book

Carter, J. A., Sembay, S., and Read, A. M. (2010). A high charge state coronal mass ejection seen through solar wind charge exchange emission as detected by *XMM-Newton*. *Mon. Not. R. Astron. Soc.*, *402*(2), 867–878. https://

doi.org/10.1111/j.1365-2966.2009.15985.x

Carter, J. A., Sembay, S., and Read, A. M. (2011). Identifying *XMM-Newton* observations affected by solar wind charge exchange—Part II. *A&A*, *527*, A115. https://doi.org/10.1051/0004-6361/201015817

Collier, M. R., and Connor, H. K. (2018). Magnetopause surface reconstruction from tangent vector observations. *J. Geophys. Res.: Space Phys.*, *123*(12), 10189–10199. https://doi.org/10.1029/2018JA025763

Connor, H. J., Raeder, J., and Trattner, K. J. (2012). Dynamic modeling of cusp ion structures. *J. Geophys. Res.: Space Phys.*, *117*(A4), A04203. https://doi.org/10.1029/2011JA017203

Connor, H. K., Zesta, E., Ober, D. M., and Raeder, J. (2014). The relation between transpolar potential and reconnection rates during sudden enhancement of solar wind dynamic pressure: OpenGGCM-CTIM results. *J. Geophys. Res.: Space Phys.*, *119*(5), 3411–3429. https://doi.org/10.1002/2013JA019728

Connor, H. K., Raeder, J., Sibeck, D. G., and Trattner, K. J. (2015). Relation between cusp ion structures and dayside reconnection for four IMF clock angles: OpenGGCM-LTPT results. *J. Geophys. Res.: Space Phys.*, *120*(6), 4890–4906. https://doi.org/10.1002/2015JA021156

Connor, H. K., Zesta, E., Fedrizzi, M., Shi, Y., Raeder, J., Codrescu, M. V., and Fuller-Rowell, T. J. (2016). Modeling the ionosphere–thermosphere response to a geomagnetic storm using physics-based magnetospheric energy input: OpenGGCM-CTIM results. *J. Space Weather Space Clim.*, *6*, A25. https://doi.org/10.1051/swsc/2016019

Connor, H. K., Sibeck, D. G., Collier, M. R., Baliukin, I. I., Branduardi-Raymont, G., Brandt, P. C., Buzulukova, N. Y., Collado-Vega, Y. M., Escoubet, C. P., ... Zoennchen, J. H. (2021). Soft X-ray and ENA imaging of the Earth's dayside magnetosphere. *J. Geophys. Res.: Space Phys.*, *126*(3), e2020JA028816. https://doi.org/10.1029/2020JA028816

Cramer, W. D., Raeder, J., Toffoletto, F. R., Gilson, M., and Hu, B. (2017). Plasma sheet injections into the inner magnetosphere: Two-way coupled OpenGGCM-RCM model results. *J. Geophys. Res.: Space Phys.*, *122*(5), 5077–5091. https://doi.org/10.1002/2017JA024104

Cravens, T. E. (1997). Comet Hyakutake X-ray source: Charge transfer of solar wind heavy ions. *Geophys. Res. Lett.*, *24*(1), 105–108. https://doi.org/10.1029/96GL03780

Cravens, T. E., Robertson, I. P., and Snowden, S. L. (2001). Temporal variations of geocoronal and heliospheric X-ray emission associated with the solar wind interaction with neutrals. *J. Geophys. Res.: Space Phys.*, *106*(A11), 24883–24892. https://doi.org/10.1029/2000JA000461

Fabian, A. C., Sanders, J. S., Allen, S. W., Crawford, C. S., Iwasawa, K., Johnstone, R. M., Schmidt, R. W., and Taylor, G. B. (2003). A deep Chandra observation of the Perseus cluster: Shocks and ripples. arXiv: astro-ph/0306036

Ferdousi, B., and Raeder, J. (2016). Signal propagation time from the magnetotail to the ionosphere: OpenGGCM simulation. *J. Geophys. Res.: Space Phys.*, *121*(7), 6549–6561. https://doi.org/10.1002/2016JA022445

Ferdousi, B., Raeder, J., Zesta, E., Cramer, W., and Murphy, K. (2021). Association of auroral streamers and bursty bulk flows during different states of the magnetotail: A case study. *J. Geophys. Res.: Space Phys.*, *126*(9), e2021JA029329. https://doi.org/10.1029/2021JA029329

Jansen, F., Lumb, D., Altieri, B., Clavel, J., Ehle, M., Erd, C., Gabriel, C., Guainazzi, M., Gondoin, P., …Vacanti, G. (2001). XMM-Newton observatory: I. The spacecraft and operations. *A&A*, *365*(1), L1–L6. https://doi.org/10.1051/0004-6361:20000036

Jensen, J. B., Raeder, J., Maynard, K., and Cramer, W. D. (2017). Particle precipitation effects on convection and the magnetic reconnection rate in Earth's magnetosphere. *J. Geophys. Res.: Space Phys.*, *122*(11), 11413–11427. https://doi.org/10.1002/2017JA024030

Jorgensen, A. M., Sun, T. R., Wang, C., Dai, L., Sembay, S., Wei, F., Guo, Y. H., Xu, R. L. (2019a). Boundary detection in threedimensions with application to the SMILE mission: The effect of photon noise. *J. Geophys. Res: Space Phys.*, *124*(6), 4365–4383. https://doi.org/10.1029/2018JA025919

Jorgensen, A. M., Sun, T. R., Wang, C., Dai, L., Sembay, S., Zheng, J. H., Yu, X. Z. (2019b). Boundary detection in three dimensionswith application to the SMILEmission: The effect of model-ittig noise. *J. Gieophys. Res: Space Phys.*, *124*(6), 4341–4355. https://doi.org/10.1029/2018JA026124

Jung, J., Connor, H. K., Carter, J. A., Koutroumpa, D., Pagani, C., and Kuntz, K. D. (2022). Solar minimum exospheric neutral density near the subsolar magnetopause estimated from the XMM soft X-ray observations on 12 November 2008. *J. Geophys. Res.: Space Phys.*, *127*(3), e2021JA029676. https://doi.org/10.1029/2021JA029676

Kavosi, S., Spence, H. E., Fennell, J. F., Turner, D. L., Connor, H. K., and Raeder, J. (2018). MMS/FEEPS observations of electron microinjections due to Kelvin–Helmholtz waves and flux transfer events: A case study. *J. Geophys. Res.: Space Phys.*, *123*(7), 5364–5378. https://doi.org/10.1029/2018JA025244

Kuntz, K. D., Collado-Vega, Y. M., Collier, M. R., Connor, H. K., Cravens, T. E., Koutroumpa, D., Porter, F. S., Robertson, I. P., Sibeck, D. G., … Walsh, B. M. (2015). The solar wind charge-exchange production factor for hydrogen. *Astrophys. J.*, *808*(2), 143. https://doi.org/10.1088/0004-637X/808/2/143

Lisse, C. M., Dennerl, K., Englhauser, J., Harden, M., Marshall, F. E., Mumma, M. J., Petre, R., Pye, J. P., Ricketts, M. J., ... West, R. G. (1996). Discovery of X-ray and extreme ultraviolet emission from Comet C/Hyakutake 1996 B2. *Science, 274*(5285), 205–209. https://doi.org/10.1126/science.274.5285.205

Misra, D., Mishra, S., and Appasani, B. (2018). Advanced image processing for astronomical images. arXiv: 1812.09702.

Oiler, J., and Rogers, A. E. E. (2020). Analysis of limb brightening on the quiet sun at 21cm using a three-element interferometer. https://www.haystack.mit.edu/wp-content/uploads/2020/07/pubs_srt_Jon-Oiler-Final-report.pdf

Oliveira, D. M., and Raeder, J. (2015). Impact angle control of interplanetary shock geoeffectiveness: A statistical study. *J. Geophys. Res.: Space Phys.*, *120*(6), 4313–4323. https://doi.org/10.1002/2015JA021147

Qin, J. Q., and Waldrop, L. (2016). Non-thermal hydrogen atoms in the terrestrial upper thermosphere. *Nat. Commun.*, *7*, 13655. https://doi.org/10.1038/ncomms13655

Raeder, J., McPherron, R. L., Frank, L. A., Kokubun, S., Lu, G., Mukai, T., Paterson, W. R., Sigwarth, J. B., Singer, H. J., and Slavin, J. A. (2001). Global simulation of the Geospace environment modeling substorm challenge event. *J. Geophys. Res.: Space Phys.*, *106*(A1), 381–395. https://doi.org/10.1029/2000JA000605

Raeder, J., Larson, D., Li, W. H., Kepko, E. L., and Fuller-Rowell, T. (2008). OpenGGCM simulations for the THEMIS mission. *Space Sci. Rev.*, *141*(1-4), 535–555. https://doi.org/10.1007/s11214-0421-5

Robertson, I. P., and Cravens, T. E. (2003). X-ray emission from the terrestrial magnetosheath. *Geophys. Res. Lett.*, *30*(8), 1439. https://doi.org/10.1029/2002GL016740

Sanders, J. S., Fabian, A. C., Russell, H. R., Walker, S. A., and Blundell, K. M. (2016). Detecting edges in the X-ray surface brightness of galaxy clusters. *Mon. Not. R. Astron. Soc.*, *460*(2), 1898–1911. https://doi.org/10.1093/mnras/stw1119

Shi, Y., Zesta, E., Connor, H. K., Su, Y. J., Sutton, E. K., Huang, C. Y., Ober, D. M., Christodoulou, C., Delay, S., and Oliveira, D. M. (2017). High-latitude thermosphere neutral density response to solar wind dynamic pressure enhancement. *J. Geophys. Res.: Space Phys.*, *122*(11), 11559–11578. https://doi.org/10.1002/2017JA023889

Shue, J. H., Chao, J. K., Fu, H. C., Russell, C. T., Song, P., Khurana, K. K., and Singer, H. J. (1997). A new functional form to study the solar wind control of the magnetopause size and shape. *J. Geophys. Res.: Space Phys.*, *102*(A5), 9497–9511. https://doi.org/10.1029/97JA00196

Sibeck, D. G., Lopez, R. E., and Roelof, E. C. (1991). Solar wind control of the magnetopause shape, location, and motion. *J. Geophys. Res.: Space Phys.*, *96*(A4), 5489–5495. https://doi.org/10.1029/90ja02464

Sibeck, D. G., Allen, R., Aryan, H., Bodewits, D., Brandt, P., Branduardi-Raymont, G., Brown, G., Carter, J. A., Collado-Vega, Y. M., … Wing, S. (2018). Imaging plasma density structures in the soft X-rays generated by solar wind charge exchange with neutrals. *Space Sci. Rev.*, *214*(4), 79. https://doi.org/10.1007/s11214-018-0504-7

Snowden, S. L., Egger, R., Freyberg, M. J., McCammon, D., Plucinsky, P. P., Sanders, W. T., Schmitt, J. H. M. M., Truemper, J., and Voges, W. (1997). *ROSAT* survey diffuse X-ray background maps. II. *Astrophys. J.*, *485*(1), 125–135. https://doi.org/10.1086/304399

Sun, T. R., Wang, C., Connor, H. K., Jorgensen, A. M., and Sembay, S. (2020).

Deriving the magnetopause position from the soft X-ray image by using the tangent fitting approach. *J. Geophys. Res.: Space Phys.*, *125*(9), e2020JA028169. https://doi.org/10.1029/2020JA028169

Trümper, J. (1982). The ROSAT mission. *Adv. Space Res.*, *2*(4), 241–249. https://doi.org/10.1016/0273-1177(82)90070-9

Walsh, B., Collier, M. R., Busk, S., Connor, H. K., Kuntz, K. D., McShane, J., Naldoza, V., Porter, F. S., Sibeck, D. G., … Thomas, N. (2020). The lunar environment heliospheric X-ray imager (LEXI)–A mission for global magnetospheric imaging. In AGU Fall Meeting. AGU.

Walsh, B. M., Collier, M. R., Kuntz, K. D., Porter, F. S., Sibeck, D. G., Snowden, S. L., Carter, J. A., Collado-Vega, Y., Connor, H. K., … Thomas, N. E. (2016). Wide field-of-view soft X-ray imaging for solar wind–magnetosphere interactions. *J. Geophys. Res.: Space Phys.*, *121*(4), 3353–3361. https://doi.org/10.1002/2016JA022348

Whittaker, I. C., and Sembay, S. (2016). A comparison of empirical and experimental O^{7+}, O^{8+}, and O/H values, with applications to terrestrial solar wind charge exchange. *Geophys. Res. Lett.*, *43*(14), 7328–7337. https://doi.org/10.1002/2016GL069914